University of Cambridge, Department of Engineering

Masters Project Report

Propulsion Systems for VTOL Electric Aircraft

Jonathan Barry

Supervised by
Dr. Sam Grimshaw
Dr. James Taylor

Abstract

This report opens with an introduction to urban air taxis (UAT's) and the engineering challenges of designing a propulsor design for efficient vertical take-off and landing (VTOL). As fully electric UAT's have recently become viable, so too have new configurations of UAT, and the main challenge identified is reducing the power usage during VTOL for a fully electric configuration.

From the literature review, a non-dimensional figure of merit, M_f is identified, which should be maximised for efficient VTOL. Using a momentum analysis, it is shown that an idealised ducted fan has a non-dimensional figure of merit of $\sqrt{2\sigma}$ for an exit nozzle of area ratio, σ. This is above that of an ideal propeller, for which $M_f = 1$. Hence, ducted fan designs are investigated in this project, with emphasis placed on reducing the total weight of the duct whilst achieving a high non-dimensional figure of merit by increasing the area ratio of exit nozzle.

To enable calculation of the non-dimensional figure of merit for different designs, this project sought to design and build a ducted fan test rig. The completed test rig allows measurement of the total thrust, power, shaft speed and a range of aerodynamic measurements from the fan. The intake and exit nozzle of the rig is fully replaceable, allowing new designs to be 3D printed, fitted and tested. With a design operating speed of 4000 RPM, the fan has a blade tip Reynold's number of $\approx 10^4$, which is comparable to that of a working scale UAT.

When tested, the baseline intake and exit nozzle case is found to have a non-dimensional figure of merit, $M_f = 1.06$. Using momentum theory and a control volume analysis, the thrust contributions from the intake, fan and the exit can be calculated. The total thrust calculated from this method shows close agreement to the measured value, with an error below 20%. Additionally, an idealised control volume analysis can also be used to calculate the predicted composition of the total thrust. When this is done, the thrust contribution calculated from the intake and fan agree closely with the theoretical values, differing by $< 10\%$.

Once calculated, the non-dimensional figures of merit are adjusted to allow for comparison between them at the peak isentropic efficiency of the fan. All non-dimensional figures of merit are calculated to be below their ideal theoretical values, and this is hypothesised to be because the real flow is not isentropic. Two short diffusing exit nozzle designs were tested, these had the same area ratio and length, but differed in that one implemented a splitter vane. The exit nozzle with a single splitter vane was not found to improve VTOL efficiency. It is therefore proposed that CFD is required to optimise a splitter design, to delay flow separation and increase the non-dimensional figure of merit.

The baseline intake and exit nozzle was found to have the highest non-dimensional figure of merit, $M_f = 1.08$. The case with the short intake and short diffusing exit

nozzle is found to have a non-dimensional figure of merit only 14.2% below this, but this is achieved with a total intake and exit nozzle weight reduction of 68.6% compared to the baseline case.

There is scope for further work on this project, and it is recommended that the functionality of the test rig is extended. These extensions will include the addition of multi-hole pressure probe traverses, used to traverse the entire entrance and exit area of the fan, in order to calculate an average static pressure rise and flow coefficient. Additionally, 2D traverses can be added to analyse the captured stream-tube entering the intake, and the exit jet leaving the exit nozzle. Furthermore, CFD is recommended for future design work on the the intake and exit exit nozzles, such as optimising a splitter vane design for a short diffusing exit nozzle.

Nomenclature

T	Thrust	N

Geometry

r_c	Casing Radius	m
r_h	Hub Radius	m
r_m	Mean-line Radius	m

Non-dimensional Properties

Λ	Reaction
ϕ	Flow Coefficient
ψ	Stage Loading Coefficient

Other Symbols

$\dot{m}$	Mass Flow Rate	$Kgms^{-1}$
$\dot{Q}$	Volumetric Flow Rate	m^3s^{-1}
σ	Exit Nozzle Area Ratio	
AR	Aspect Ratio	
P	Electrical Power	W

Subscripts

$()_0$	Upstream Far-field
$()_1$	Intake Entrance
$()_2$	Intake Exit
$()_3$	Exit Nozzle Inlet
$()_4$	Exit Nozzle Outlet
$()_5$	Downstream Far-field
$()_c$	Casing
$()_h$	Hub
$()_m$	Mid-span
$()_r$	Rotor Blade
$()_s$	Stator Blade
$()_T$	Total
$()_x$	Axial

Contents

1 Introduction

1.1 Urban Air Taxis

With increased strain on transport infrastructure [1], there is interest in the development of light aircraft for use in heavily urbanised areas and cityscapes. These urban air taxis (UAT's) will be capable of vertical take-off and landing (VTOL), enabling the transport of passengers without the need for expensive infrastructure such as runways. Furthermore, progress has been made on developing a competent regulatory framework for the operation of UAT's, such as by the European Aviation Safety Agency (EASA) [2]. With the recent advances in electric battery technology [3], fully electric UAT's are now viable, and with that new configurations are possible using electric propellers or ducted fans for propulsion.

One configuration, known as a tilt-wing, consists of electric propellers mounted on rotating wings, with a recent example of this configuration being the Rolls Royce concept UAT. This is shown in VTOL configuration in Figure 1a, utilising vertically orientated propellers for efficient VTOL. Therefore, when rotated back to their forward position the aerofoils allow for efficient forward flight of the UAT as shown in Figure 1b. Unlike designs in which the wings are fixed, the majority of the wing area of a tilt-rotor lies within the exit slipstream of the propeller [5]. This means that the area of the wing enclosed by this slipstream will not stall when transitioning from VTOL to forward flight. The increased flow velocity across the wing is also shown to increase lift at low forward velocities during transition [6].

(a) VTOL configuration

(b) Forward flight configuration

Figure 1: A concept UAT unvieled by Rolls Royce at the Farnborough airshow 2018 [4]

There are a number of technical challenges to overcome before UAT's are adopted on a large scale. One key challenge is minimising power usage during VTOL, whilst still providing sufficient thrust for hovering. In this section there will be a literature review, which includes consideration of a non-dimensional figure of merit for VTOL, propellers, ducted fans, and methods for improving ducted fans. This is followed by a description of the project objectives and structure of the report.

1.2 Literature Review

1.2.1 Comparison of Propulsor Performance

A comparison of the hovering performance of different propulsor designs was completed by the Hiller Aircraft Corporation [7], during which they defined several performance metrics. Firstly, they defined the performance metric $\frac{T_T}{P}$ as a measure of VTOL efficiency, where thrust, T_T is normalised by power, P. Additionally, as rotor area is a practical concern, a second performance metric of $\frac{T_T}{A}$ can be used, where thrust, T_T is normalised by rotor area, A. Dimensional analysis can be used to derive a non-dimensional figure of merit, M_f, given by Equation (1), combining these two performance metrics.

Different propulsor designs can be plotted on a graph of $\frac{T_T}{P}$ against $\frac{T_T}{Ac}$ as in Figure 2. Contours of M_f are plotted and this shows that for a fixed $\frac{T_T}{P}$, increasing M_f allows the same thrust to be achieved with a smaller rotor area. Also for a fixed $\frac{T_T}{A}$, increasing M_f allows the same thrust to be achieved with a reduced power requirement. Hence, when designing the electric propulsor for the UAT we should aim to maximise M_f.

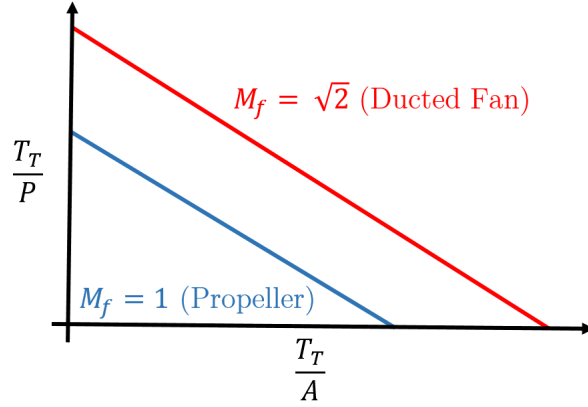$$M_f = \frac{T_T}{P} \sqrt{\frac{T_T}{2\rho A}} \tag{1}$$

Figure 2: Figures of merit of various different fan designs, adapted from [7]

1.2.2 Figures of merit for Ducted and Non-ducted Fans

Using a control volume method and momentum theory we can evaluate M_f for both a propeller and a ducted fan by assuming that the flow is steady, inviscid, incompressible, and has no exit swirl [8]. For a propeller, assumed to have no exit stream tube diffusion, M_f is 1. Unlike a propeller, the exit nozzle of a ducted fan can be used to vary the ratio of the nozzle exit area to the annulus area, σ which is defined in Equation (2). For a ducted fan with a diffuser the total thrust is then given by Equation (3) and the total shaft power

by Equation (4). Combining Equations (3) and (4), the non-dimensional figure of merit for a ducted fan is given by Equation (5).

$$\sigma = \frac{A_{Jet}}{A_x} \tag{2}$$

$$T_T = \frac{\rho A_x V_x^2}{\sigma} \tag{3}$$

$$P = \frac{\rho A_x V_x^3}{2\sigma^2} \tag{4}$$

$$M_{f,Ducted} = \sqrt{2\sigma} \tag{5}$$

This result shows that in the case of no exit diffusion, the non-dimensional figure of merit of a ducted fan is a factor of $\sqrt{2}$ larger than that of a propeller. It also suggests that the non-dimensional figure of merit can be further increased using a diffuser for an exit nozzle with an area ratio, $\sigma > 1$. Therefore, ducted fans are expected to be more suitable for use in a UAT in the VTOL configuration, and hence improving their performance is the focus of this research project.

1.2.3 Problems with Ducted Fans

Despite ducted fans having a theoretical VTOL efficiency, there are practical issues with their use, meaning propellers are currently more prevalent in UAT concept designs.

Whilst it has been shown that using a diffuser with a large area ratio, σ can improve the VTOL efficiency, this also presents practical problems. As the area of the diffuser increases we expect the flow velocity to decrease for continuity of the mass flow rate, and therefore using Bernoulli's equation for incompressible inviscid steady flow along a streamline, we expect the static pressure of the flow to increase. This adverse pressure gradient can therefore cause the boundary layer to separate from the inside wall of the exit nozzle.

To reduce the risk of separation, ducted fans often have a long exit nozzle. When the area ratio, σ is fixed, reducing the diffuser length causes a more extreme adverse pressure gradient, which makes separation more likely. This also means that the additional weight of ducting reduces the effective thrust during VTOL, and this problem scales as the fan radius increases. Additionally, the intake of a ducted fan is prone to separation due to cross-winds as shown in Figure 3, which changes the direction of the thrust vector. For these reasons large radius ducted fans are often a more expensive option with less reliable thrust vectoring, and hence large radius propeller designs are often favoured.
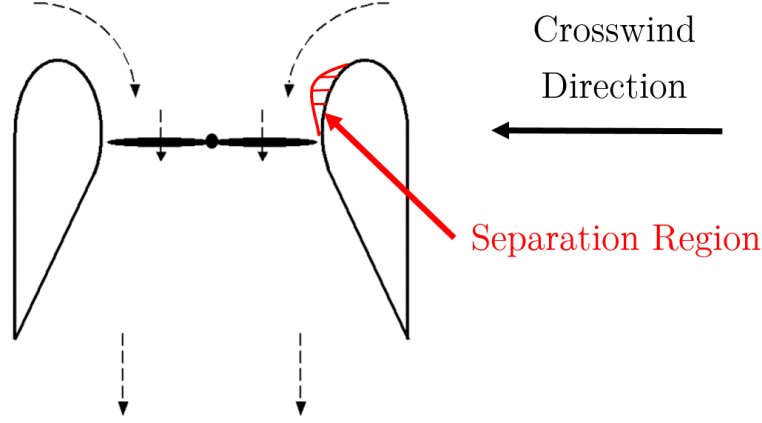
Figure 3: An illustration of intake separation on a ducted fan

1.2.4 Design Improvements for Ducted Fans

As wind tunnel testing is not possible within the time-scale of this project, the effect of cross-winds on the intake will not be investigated. However, the effect of shortening the intake on the flow field and its contribution to the total thrust will be investigated.

In order to reduce or eliminate the detrimental effects of boundary layer separation in a diffusing exit nozzle, several novel designs will be tested. If successful, these designs should delay separation, allowing aggressive diffusing exit nozzles to be used which is expected to increase the non-dimensional figure of merit for the ducted fan. Each design feature will therefore be tested in isolation before various combinations of design features are tested.

1.2.5 Splitter Vanes

Splitter vanes have been implemented as a means of secondary flow control in low aspect ratio turbine stator rows to split the diffusion of highly loaded components [10]. These splitters gave a reduction in end-wall losses and were found to increase stage efficiency of a low-speed turbine stage by 0.88%. It has also been shown that implementing splitter vanes in S-shaped ducts can reduce end wall loading and delay boundary layer separation [11].

This splitter concept can also be implemented in both the intake and exit nozzle of a ducted fan as illustrated in Figure 4. For a diffusing exit nozzle, splitter vanes will delay or prevent boundary layer separation in the exit nozzle. Hence, the non-dimensional figure of merit will increase due to the increased area ratio, σ, whilst also reducing the length and therefore total weight of the exit nozzle.
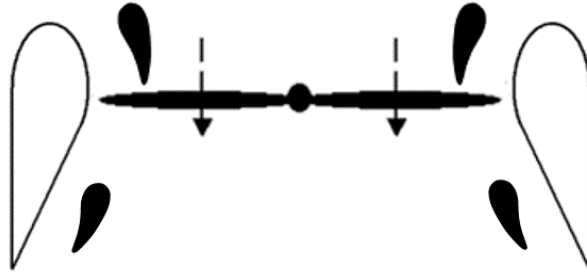
Figure 4: Example of a ducted fan implementing splitter vanes

1.3   Project Objectives and Report Structure

The primary objectives of the research project are to:

1. Design and build an experimental rig for testing intake and exit nozzle designs on a ducted fan

2. The intake and exit nozzle must be replaceable

3. The rig must allow the non-dimensional performance metric of different designs to be determined

4. To determine ways of increasing the non-dimensional performance metric, M_f of a ducted fan

5. Address the practical problems for the implementation of ducted fans, including:

   - Reduced effective thrust due to duct weight

   The experimental design and methodology for the test rig is detailed in Section 2. The results are presented in the following sections:

1. Baseline intake and exit nozzle tests

2. Modifications to the exit nozzle and intake

3. Combined design improvements

4. Conclusions

5. Future work

2 Experimental Design and Methods

In order to test duct designs on an electric fan, a test rig was designed and built at the Whittle Laboratory. This section details the design of the test rig, measurement methods and the experimental procedure used for data acquisition. Furthermore, this section also includes an overview of the intake and exit nozzle designs for the fan which were subsequently tested.

2.1 Concept Design

The ducted fan consists of the rotor, mounted on an electric motor, which is then fitted onto the fixed stator section of the fan such that the stator casing wall encloses the rotor. This is illustrated by the cross-section of the ducted fan in Figure 5 which shows the baseline intake, exit nozzle, intake cone and exit cone designs fitted.

The test rig has been designed to allow different intakes and exit nozzles to be easily fitted and removed. As shown in the cross-section, the intake and exit nozzle are split such that they can be fitted around railings on the stator section before being secured together using screws. This allows rapid prototyping of intake and exit nozzle designs which can be 3D printed in sections before being assembled for testing.
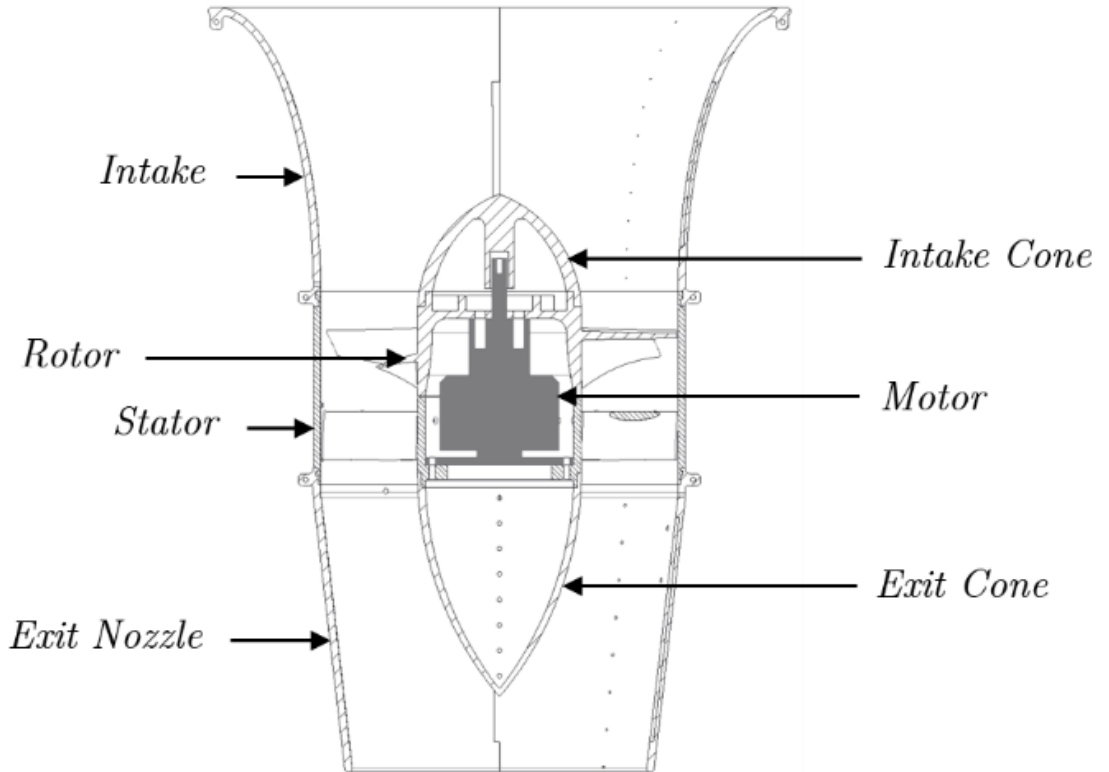

Figure 5: Annotated cross-section of the ducted fan

2.2 Propulsor Rig

2.2.1 Turbomachinery

The ducted fan uses a blade geometry developed previously by the author during a summer research project, with the design parameters summarised in Table 1 [18]. As the ducted fan essentially operates as an axial compressor stage, the boundary layer on the blades may separate due to adverse pressure gradient [15]. The blades use a front-thickened profile which has been shown to delay turbulent separation for low Reynold's number compressor blades [13]. Furthermore, the fan has been designed using a mean-line approach [17] for an operating speed of 4000 RPM which will give a blade-tip Reynolds number of $\approx 10^4$, assuming international standard atmospheric conditions at sea level, which is comparable to the working scale flow regime of a UAT. Another design feature is that the blade profiles have been designed to have no entry and exit swirl. This means that provided the curvature of the intake and exit nozzles is low close to the turbomachinery, the flow can be assumed to be axial with no radial pressure gradient.
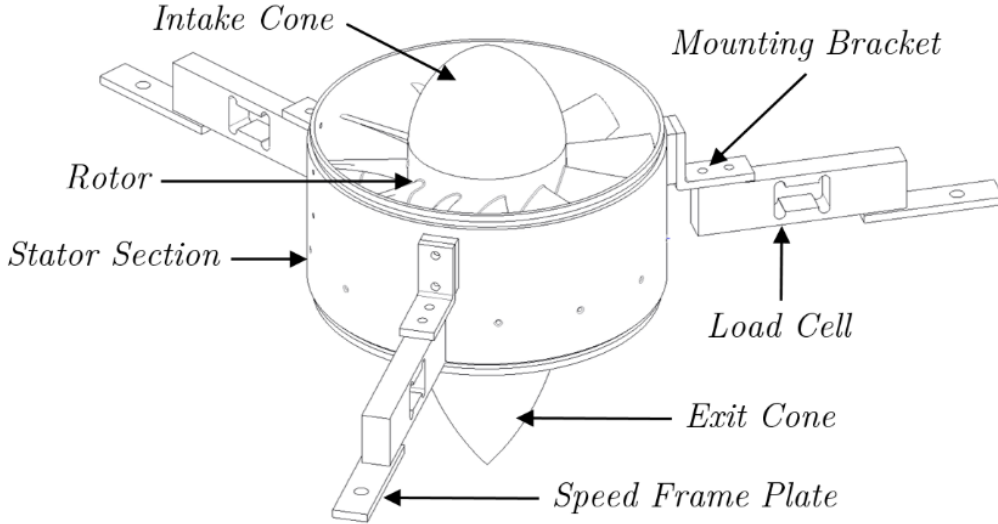

Figure 6: Annotated diagram of the ducted fan with no intake or exit nozzle fitted

The rotor and stator sections of the turbomachinery were constructed from Polyamide (PA) polymer using selective laser sintering before finishing. An intake cone and exit cone were 3D printed from polylactic acid (PLA) polymer and fitted onto the rotor and stator respectively as shown in Figure 6. the cross-section in Figure 5 shows how the intake cone screws on to motor, locking it to the rotor section, whilst the exit cone is attached to the stator section using a mechanical friction fit. During finishing, a matte black paint coating was applied to the rotor, intake and exit cones to improve the surface finish and allow for optical sensors to be used on the rotor for measuring the rotational speed of the shaft.

Geometry			Operating Point		
Parameter	Value	Units	Parameter	Value	Units
r_h	0.055	m	ϕ	0.6	N/A
r_c	0.12	m	ψ_{s-s}	0.7	N/A
r_m	0.0875	m	Λ	0.825	N/A
AR_r	1.8	N/A	Ω	6000	RPM
AR_s	1.8	N/A	P	547	W

Table 1: Design parameters for the fan design

2.2.2 Drive System

The ducted fan is powered by a brushless DC motor, the base of which is secured to the stator section of the assembly. The rotor is attached to the motor outrunning section. Various parameters for the motor, for both its rated performance and the expected value at the design operating point, are summarised in Table 2. This shows that the design operating power is $\approx 10.3\%$ of the rated power and hence the motor could be fully enclosed without the need for active cooling.

Parameter	Rated Value	Operating Value	Units
$Voltage$	44	23.3	V
$Current$	120	23.5	A
$Power$	5300	547	W

Table 2: Electric motor parameters used in the ducted fan

Power is supplied to the motor from an external electronic speed controller (ESC), which supplies three pulse-width modulated driving signals to the motor controlling its speed. These power cables are passed through the inside of the hollow stator blades and into the base of the motor. The speed of rotation of the fan is set using a rotational dial on an RC motor servo tester which is connected to the external ESC.

All power supplied to the ESC and the motor comes from a single enclosed AC-DC converting power supply, which is connected to the mains power supply. This supplies the speed controller with 36 V (DC) at a rated power of 2 kW, and includes an emergency stop switch accessible to the operator during testing.

2.2.3 Intake and Exit Nozzle

As discussed, one of the key design features of the test rig is that it allows different intake and exit nozzle designs to be fitted and replaced. All intake and exit nozzle designs were 3D printed from PLA in four sections, these were then secured together using machine screws and bolts, holding them securely around the railings on the stator section of the fan. Additionally, the intake and exit cones are also replaceable, but have been kept constant throughout testing as their design is beyond the scope of this project. The intake, exit nozzle and exit cone are designed with static pressure tappings placed axially along their length, normal to the inner wall surfaces. The use of these static pressure tappings in the measurement of the flow profile is discussed in Section 2.3.1.

Two intake designs are tested; both have an elliptic wall profile with varying axial length and inlet area. Annotated cross-sections of these designs are shown in Figure 7, and annotated cross-sections of the different exit nozzle designs tested can be found in Figure 8, with the ratio of exit to inlet area for each nozzle, σ displayed for each design.
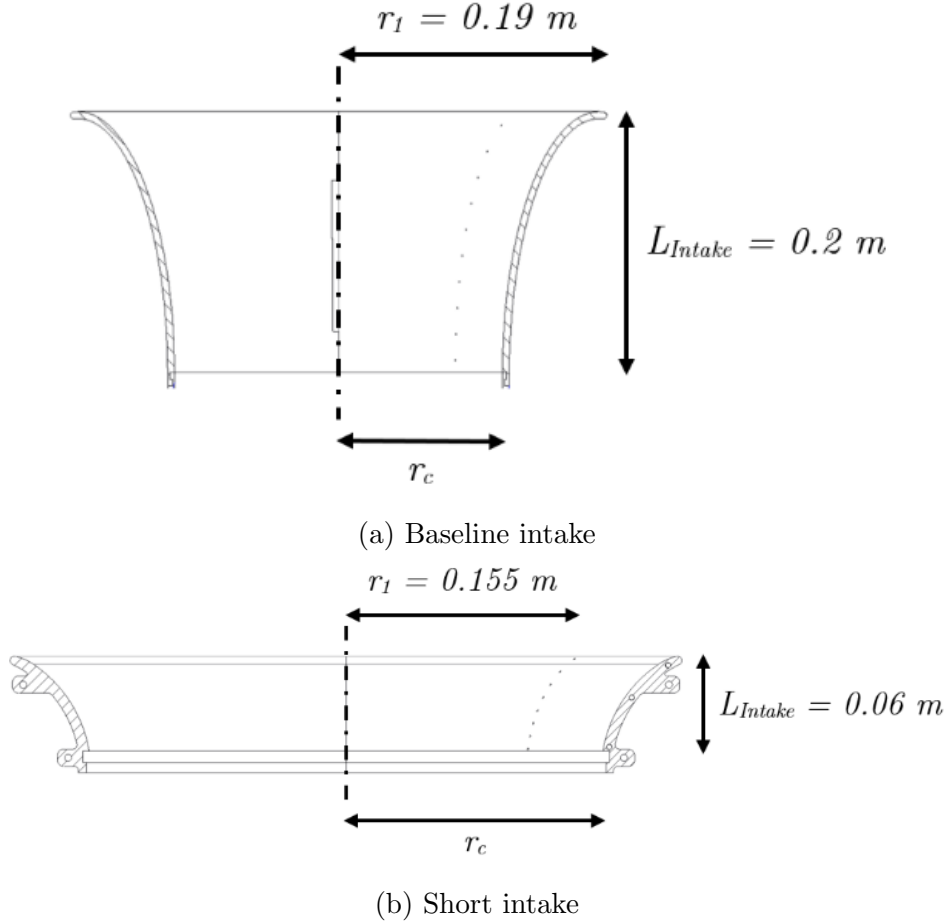

(a) Baseline intake

(b) Short intake

Figure 7: Annotated cross-sectional diagrams of intake designs tested

(a) Baseline Exit Nozzle

(b) Short exit nozzle

(c) Diffusing Exit Nozzle

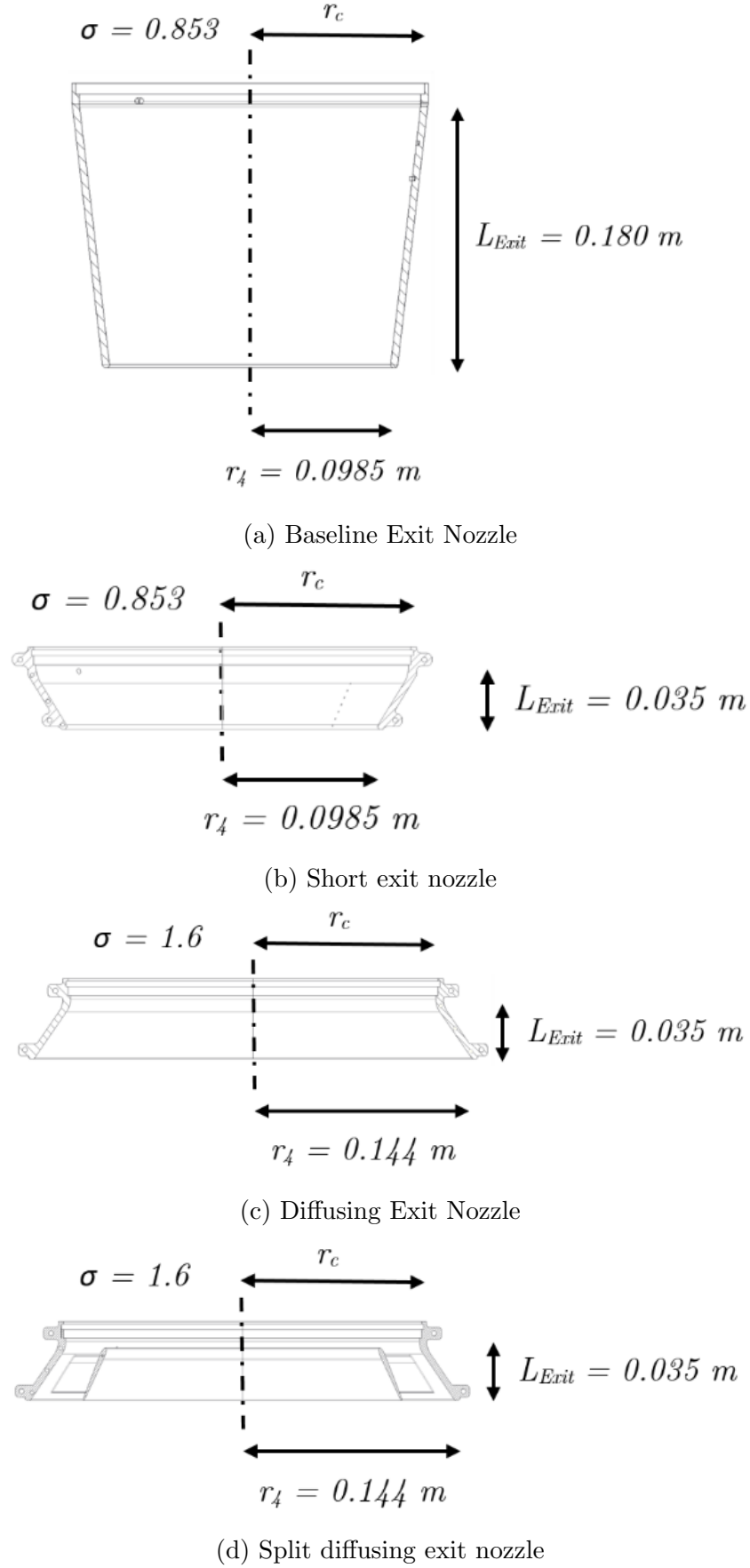
(d) Split diffusing exit nozzle

Figure 8: Annotated cross-sectional diagrams of all of the exit nozzle designs tested

2.2.4 Overall Assembly

A photo of the fully assembled test rig can be seen in Figure 9, highlighting how the load cells are rigidly connected to the mild steel speed frame plates. These speed frame plates are then secured to aluminium speed frame, which can be reconfigured to suit the testing requirements. The ESC and throttle are both mounted on the surrounding speed frame, with the external power supply for the rig contained in a metal enclosure. The static pressure tapping tubing can also be seen, and its weight is supported by the speed frame such that it will not interfere with thrust measurements.
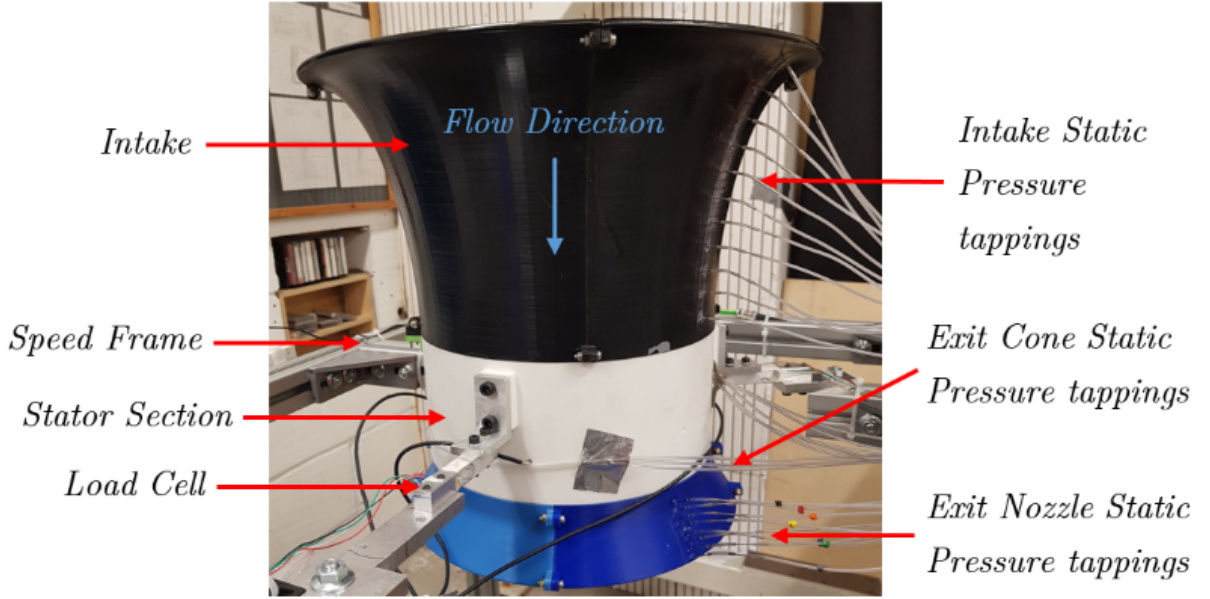

Figure 9: Annotated picture of the fully assembled ducted fan rig with baseline intake and diffusing exit nozzle fitted

2.2.5 Rotor Clocking and Balancing

Once the rotor and motor are assembled, a dial gauge is mounted on the speed frame and used to clock this partial assembly to the stator section as shown in Figure 10. This is done to minimise the offset of the rotor and stator axis, which will ensure there will be a sufficient tip gap to prevent the rotor blades from rubbing on the stator casing. The rotor was successfully clocked to the stator with a maximum radial displacement of 0.1 mm, resulting in a tip clearance of 0.3 to 0.5 mm, which is $\approx 0.6\%$ of the total blade span.

Once clocked, an accelerometer and balancing routine are used to measure the imbalance of the rotor using a trial mass. The required correction mass and phase are calculated and added to the rotor disk. This has the effect of reducing the out of balance reaction force on the rotor to $< 10\%$ of its initial value.
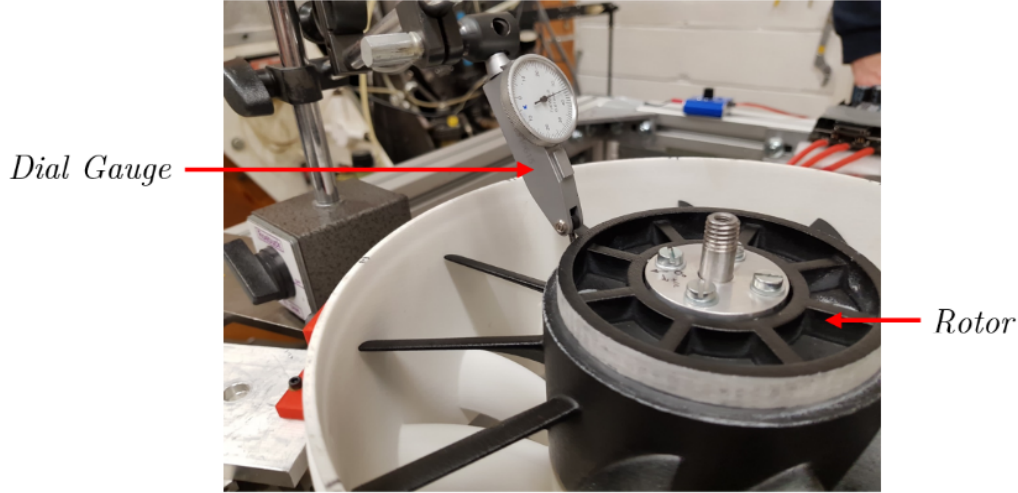
Figure 10: Dial gauge used to clock the assembled motor and rotor to the inside of the stator section

2.3 Measurement Techniques

The test rig allows measurements to be made of static pressures, the rotational speed of the fan, the electrical power from the supply and the total thrust. All of the data, excluding the pressure measurements, are logged on a desktop PC using a National Instruments data acquisition card and analysed using Matlab.

2.3.1 Pressure Measurements

Static pressure tappings were placed axially along the inside surface of the intake as shown in Figure 11, and similarly in the exit nozzle and the exit cone, allowing the pressure profiles along these surfaces to be measured. Furthermore, for the baseline intake and exit, which are assumed to have uniform velocity profiles when entering and leaving the compressor, the static pressure tappings are then used to calculate the static pressure rise across the fan.

In the absence of any separation bubbles present in the static pressure profile of the intake, the flow throughout the intake is assumed to be isentropic. Therefore, with the assumption that the flow is incompressible throughout the rig and inviscid in the intake, Bernoulli's equation can be used to calculate the axial velocity at the compressor entrance. This is because the total stagnation pressure will be approximately constant and equal to the atmospheric pressure in the intake.

All static pressures were logged on desktop PC using a 16 channel pressure scanner with a full scale long term accuracy of $\pm 0.05\%$.
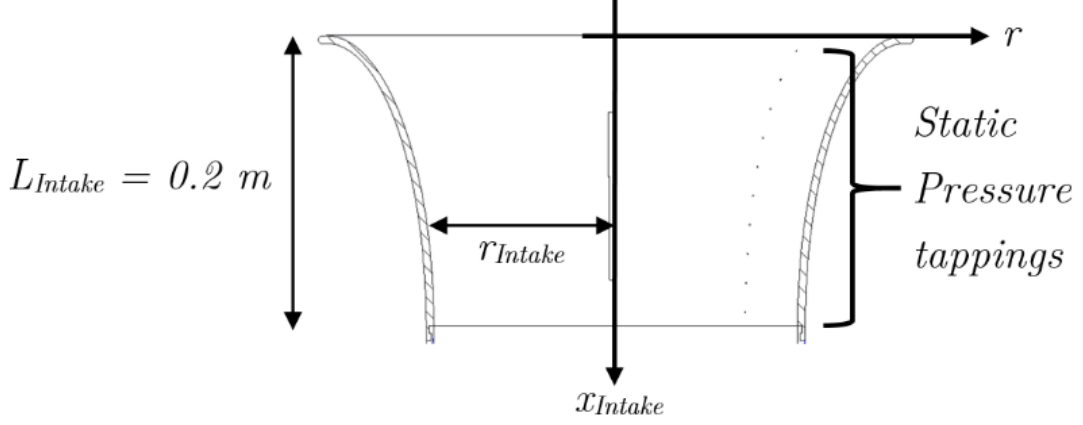
Figure 11: An annotated diagram of the static pressure tappings and nomenclature for the baseline intake

2.3.2 Shaft Speed Measurement

The shaft speed of the fan is measured using an infra-red once-per-revolution optical sensor mounted on the outside casing of the stator section. This sensor detects a thin aluminium strip placed on the rotor surface through a small hole in the stator casing, producing a periodic square wave signal. Processing this square wave signal, the shaft speed of the fan is calculated and displayed in real time on a desktop PC, allowing it to be set before measurements are taken.

2.3.3 Power Measurement

The total power supplied to the ESC and therefore the motor is measured directly from the external power supply and logged. As the efficiency of the ESC is not known, the power measured is assumed to be the total shaft power when calculating the isentropic efficiency and the non-dimensional figure of merit.

2.3.4 Thrust Measurement

Whilst the ducted fan has been mounted on three identical load cells so that the stiffness of the supports are matched, only one was used to measure the total thrust, T_{Total} of the rig. This load cell is calibrated using trial weights and a linear characteristic is found to fit the data, as shown in Figure 12, with an R-squared statistic value of 0.999. Therefore, by measuring the initial voltage offset, V_0 of the load cell at the start of each test, the total thrust is found using eq. (6).
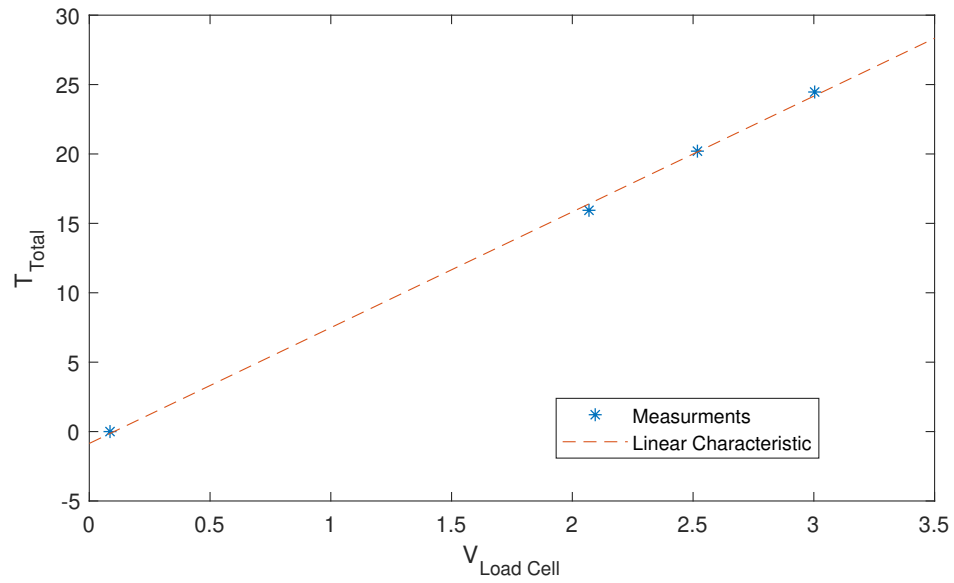
$$T_{Total} = 8.34 V_{LoadCell} + V_0 \tag{6}$$

Figure 12: The total thrust of the fan against the voltage from the load cell, showing measured values and the linear characteristic

3 Propulsor Performance with Baseline Ducts

The first set of tests were carried out with the datum intake and exit nozzle designs to validate the measurement techniques and to characterise the performance of the fan.

3.1 Control Volume Analysis

In order to determine various flow parameters, it is useful to consider a control volume enclosing the entire working section of the fan rig as shown in Figure 13. It is shown in Appendix B that for a stationary fan, where it is assumed $V_0 = 0$, that the steady flow momentum equation can be used to find an expression for the total thrust, given by Equation (7).
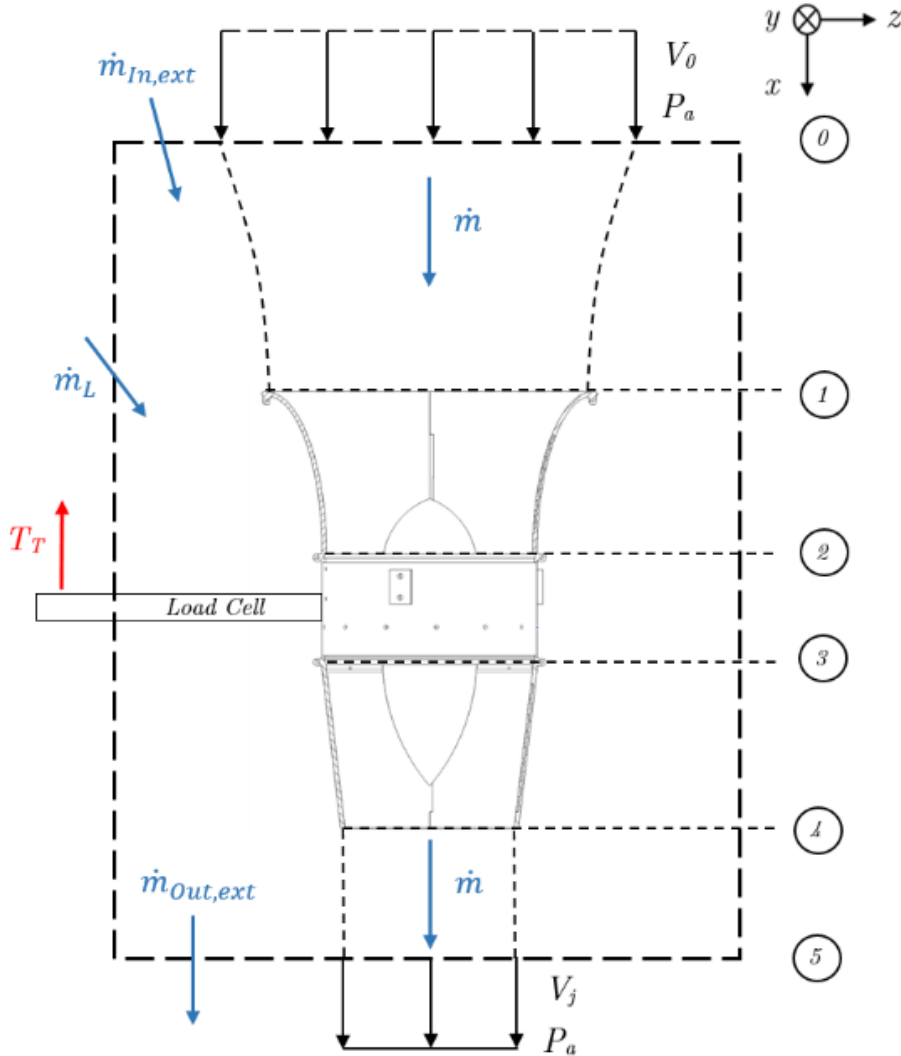

Figure 13: Control volume enclosing the entire ducted fan used to calculate total thrust

It is also assumed that the exit jet streamlines are straight and parallel, that the static pressure of the jet is atmospheric and the area of the jet is the same as that of the exit.

This allows mass flow continuity to be used to express the total thrust in terms of the axial velocity at the fan inlet, V_x, leading to an expression for the total thrust given by eq. (8), based on aerodynamic measurements.

$$T_T = \dot{m}(V_j - V_1) = \dot{m}V_j \tag{7}$$

$$\Rightarrow T_T = \frac{\rho A_{Pass} V_x^2}{\sigma} \tag{8}$$

3.2 Flow Coefficient

The non-dimensional flow coefficient through the annulus of the fan, ϕ can be calculated in two ways using the available data after a test run. One method is to assume that the flow through the intake is isentropic, and therefore the total stagnation pressure of the flow is constant and atmospheric throughout the intake. This approximation is valid based on the intake pressure profile in Figure 14 which displays no regions of flow separation. Combined with the assumption of no radial pressure gradient at the fan entrance, the flow coefficient is calculated using the gauge pressure as in Equation (9). For the baseline intake and exit nozzle, a value of $\phi = 0.62$ is calculated.

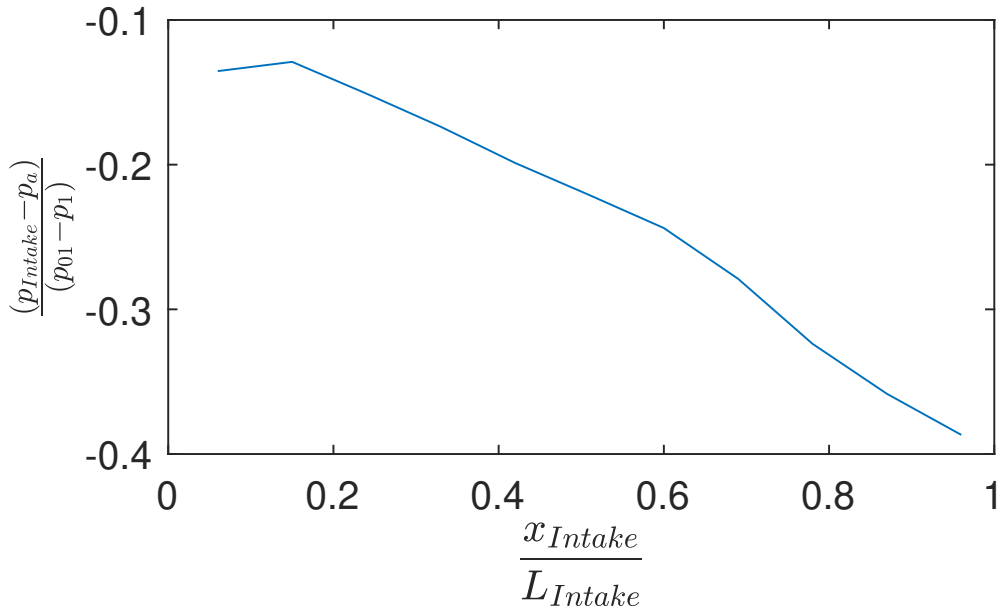$$\phi = \frac{V_x}{U} = \sqrt{\frac{(p_2 - p_a)}{\frac{1}{2}\rho U^2}} \tag{9}$$

Figure 14: Axial static pressure profile measured on the baseline intake

The intake pressure profile in Figure 14, shows a decreasing gauge pressure from $\frac{x_{Intake}}{L_{Intake}} = 0.17$ to $\frac{x_{Intake}}{L_{Intake}} = 0.95$ indicating the flow is accelerating as it approaches the

fan entrance, from Bernoulli. There is a small increase in pressure from $\frac{x_{Intake}}{L_{Intake}} = 0$ to $\frac{x_{Intake}}{L_{Intake}} = 0.17$, which suggests there is a small separation bubble at the lip of the intake.

An alternative method for calculating the flow coefficient, is to rearrange the equation for the total thrust (Equation (8)) to give eq. (10). In other words, the flow coefficient can also be calculated from the measured thrust and the nozzle exit area. From this we obtain, $\phi = 0.62$ which is equivalent to the previously calculated value to 2 significant figures, and therefore verifies the accuracy of the calculation of the flow coefficient from the measured gauge pressure for the baseline intake.

$$\phi = \sqrt{\frac{\sigma T_T}{\rho A_{Pass} U^2}} \tag{10}$$

With the known flow coefficient in the annulus calculated using the aerodynamic measurements, an alternative rearrangement of eq. (8) is used to calculate the area ratio of the exit nozzle (eq. (11)). This gives, $\sigma = 0.848$ which is 0.64% below the design value, therefore verifying the validity of assuming the exit jet area is equal to the exit area for the baseline exit nozzle. This is as expected, as the axial pressure profile of the baseline exit nozzle shown in Figure 15 indicates that the boundary layer remains attached throughout. Additionally, this also shows that the static pressure of the exit jet is approximately atmospheric, further validating the assumption of straight and parallel exit streamlines.

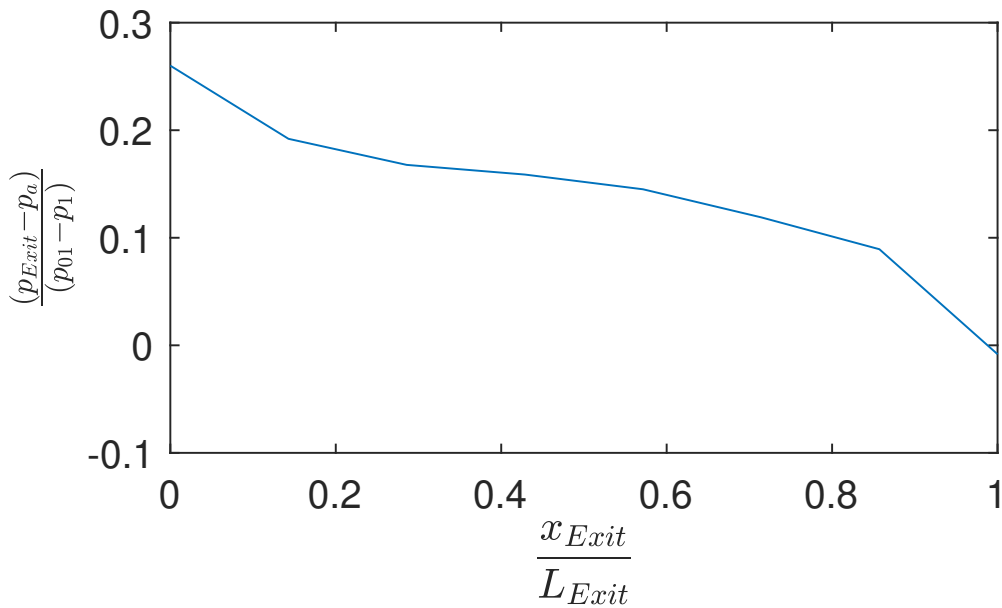$$\sigma = \frac{\rho A_{Pass} V_x^2}{T_T} \tag{11}$$

Figure 15: Axial static pressure profile measured on the baseline exit nozzle

3.3   Fan Characteristics

When the intake and exit nozzle of the ducted fan are changed, the operating point of the fan changes. Therefore, fan performance with the baseline intake and exit nozzle is characterised by throttling the exit nozzle. This allows the effect of reduced fan efficiency, when the operating point changes, to be accounted for when comparing the non-dimensional figure of merit as explained in Section 3.5.

   To change the operating point of the ducted fan, the exit area, A_4 of the baseline exit nozzle is changed by placing concentric rings over the exit plane of the exit nozzle to constrict the flow. This throttles the fan, which reduces the mass flow rate and therefore the flow coefficient.

3.3.1   Stage Loading Coefficient

The stage loading coefficient is a non-dimensional measure of the loading of a turbo-machinery stage [17]. The stage loading coefficient of the fan is calculated using the measured static-to-static pressure rise across the fan, as given by the approximation in Equation (12). This approximation relies on the assumption that the flow through the fan is approximately isentropic, and hence the thermodynamic definition of entropy in Equation (13) can be shown to simplify to an approximate relationship between the static enthalpy change and the static pressure change across the fan.

$$\psi_{s-s} = \frac{\Delta h}{\frac{1}{2}U^2} \approx \frac{p_3 - p_2}{\frac{1}{2}\rho U^2} \tag{12}$$

$$Tds = dh - \frac{1}{\rho}dp \Rightarrow \Delta h \approx \frac{1}{\rho}\Delta p \tag{13}$$

   For the baseline exit nozzle, the fan exit static pressure, p_3 is calculated by application of Bernoulli's equation to a streamline in the exit nozzle (Equation (14)). When the throttle is added to the baseline exit nozzle, the exit flow is disrupted and we can no longer apply Bernoulli's equation to the flow in the exit nozzle as it is no longer isentropic. There is a static pressure tapping at the fan exit but using this to calculate the stage loading coefficient gives a value 20.1% above the value calculated using Equation (14). It is hypothesised that this is because the tapping is in the nozzle and not in the parallel section. The streamline curvature therefore increases the pressure on the casing causing the higher value to be measured. To use this tapping a calibration factor is calculated for the baseline exit nozzle (Equation (15)), and then used to correct the static pressure measurements from this tapping for the throttled cases using Equation (16).

$$p_{3,Bernoulli} = p_a + \frac{1}{2}\rho(V_j^2 - V_x^2) \tag{14}$$

$$C_{Corr} = \frac{p_{3,Bernoulli} - p_{3,Measured}}{\frac{1}{2}\rho V_x^2} \tag{15}$$

$$p_{3,Corrected} = p_{3,Measured} + \frac{1}{2}\rho V_x^2 C_{Corr} \tag{16}$$

Once sufficient operating points are tested using the throttling procedure, the static-to-static stage loading is plotted as a function of flow coefficient as shown in Figure 16. Also displayed is the design operating point calculated from the quasi-3D blade design. This shows that the quadratic fit predicts a stage loading which is 17.4% below the designed operating point value at the operating point flow coefficient. It is hypothesised that this is because the design calculation does not include real effects such as tip clearance flows and 3D corner separations. The pressure rise across the fan is shown to increase as the flow coefficient is reduced until the fan stalls for $\phi < 0.45$. At this point the sound of the fan changes and, and the rig vibration increases.
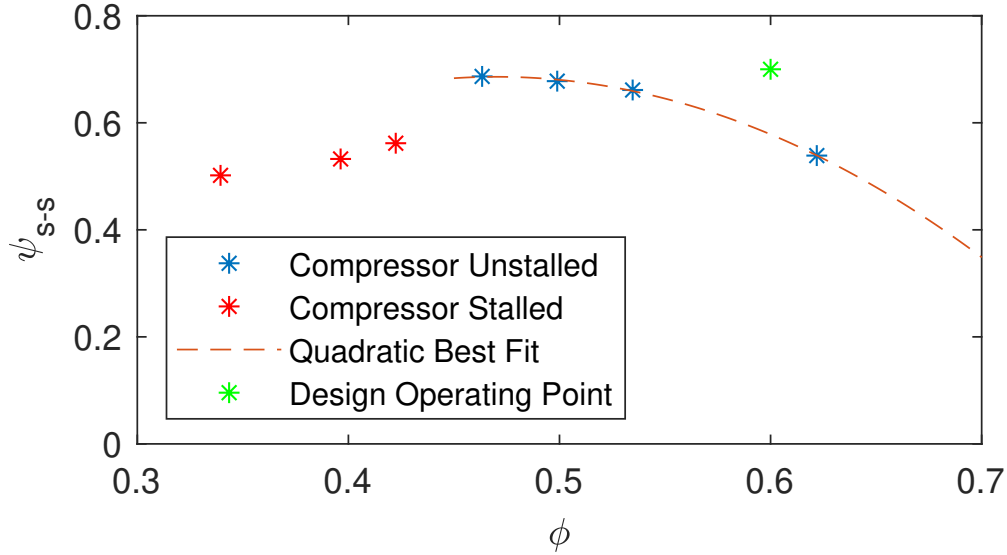

Figure 16: The static to static stage loading of the fan against flow coefficient

Another parameter of interest is the non-dimensional total thrust, T_{ND} which is calculated using Equation (17), and is plotted in Figure 17. This also increases as the flow coefficient is reduced up to the point at which the fan stalls.

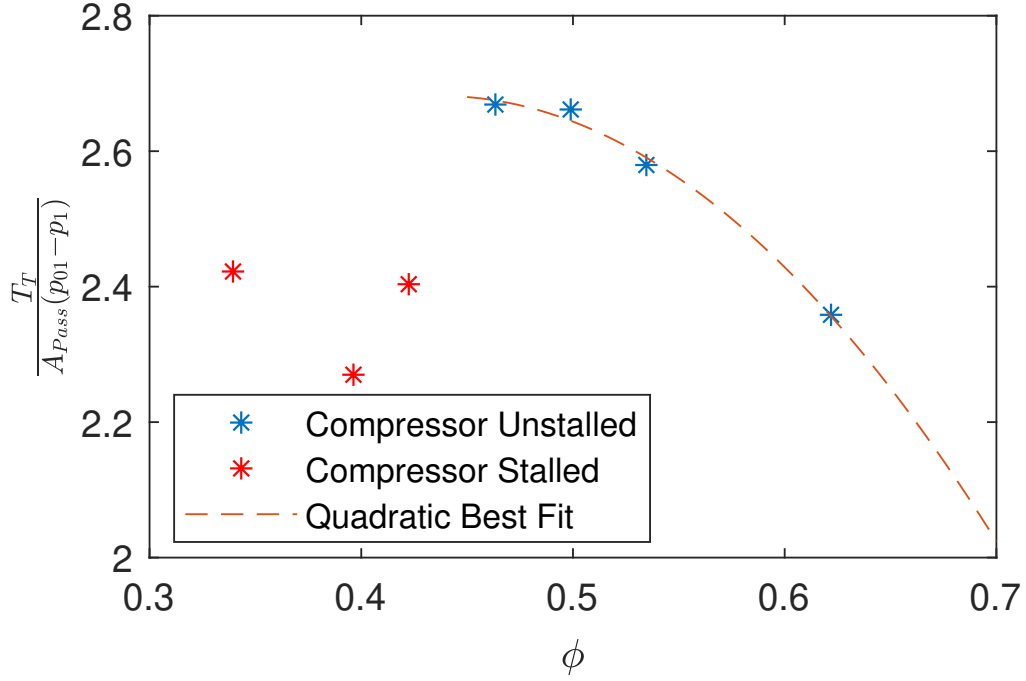$$T_{ND} = \frac{T_T}{A_{Pass}\frac{1}{2}\rho V_x^2} \tag{17}$$

Figure 17: Non-dimensional total thrust of the fan against flow coefficient

3.4 Isentropic Efficiency of Fan

The isentropic efficiency of the fan is calculated using eq. (18) [17], where the numerator is the ideal power needed for isentropic compression. In the denominator, P is the total measured electrical power supplied to the ESC and motor.

$$\eta = \frac{\dot{m}\Delta p_0}{\rho P} = \frac{\dot{m}(p_3 - p_a + \frac{1}{2}\rho V_x^2)}{\rho P} \tag{18}$$

The isentropic efficiency is calculated for various operating points and the efficiency characteristic is plotted in Figure 18, with a quadratic curve fit to the data. Interpolating using the curve fit gives a peak isentropic efficiency for the fan, $\eta_{Peak} = 83\%$ when $\phi = 0.58$, decreasing as the flow coefficient is reduced to 74% at the point of fan stall.
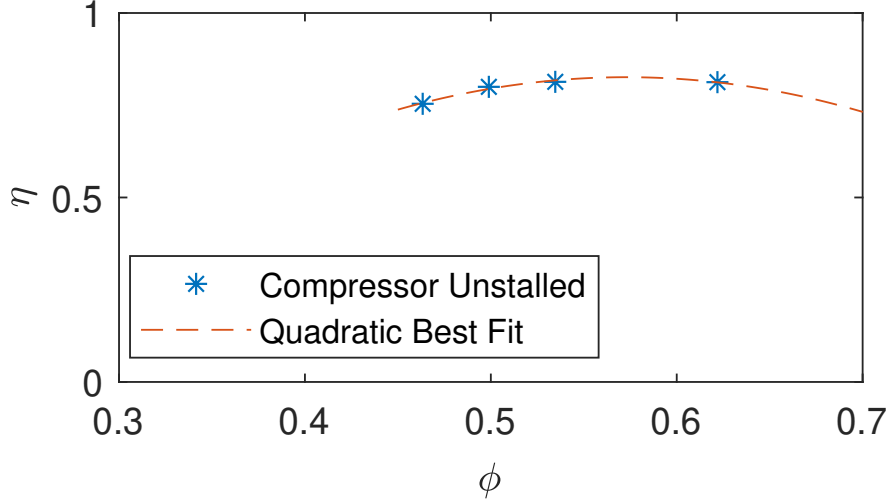
Figure 18: Isentropic efficiency of the fan against flow coefficient

3.5 Non-Dimensional Figure of Merit

For the baseline intake and exit nozzle, the non-dimensional figure of merit is calculated using Equation (1) to be 1.06. This is 18.9% below the theoretical value for a ducted fan of this area ratio (Equation (5)).

3.6 Thrust Decomposition

The total thrust of the ducted fan can be decomposed into the thrust contributions of the intake, fan section and the exit nozzle as in Equation (19). This requires a separate control volume analysis for each of these sections, allowing the thrust from each control volume to be calculated from the aerodynamic measurements.

$$T_{Total} = T_{Fan} + T_{Intake} + T_{Exit} \tag{19}$$

The thrust contribution of the intake is calculated using the control volume enclosing the captured stream-tube, shown in Figure 19. Application of the steady flow momentum equation in the axial direction gives Equation (20), which includes pressure forces acting on the flow. It can be shown using a control volume analysis and Bernoulli's equation that the pressure forces acting on the enclosed streamlines from plane 0 to plane 1 in Figure 19 causes no net axial force [12]. However, the static pressures acting on the control volume from plane 1 to plane 2 will cause an axial force. These pressure forces are calculated using a numerical integration method, described in Appendix C, using the known geometry and measured static pressures. As static pressure tappings cannot be placed on the rotating intake cone, the pressure forces acting on the cone surface have been neglected. The momentum term $\dot{m}V_x$ in Equation (20) is calculated using the flow coefficient calculated from the aerodynamic measurements in the intake.

$$T_{Intake} = [pA]_{Intake} + [pA]_{Intake,Cone} + \dot{m}V_x + (p_2 - p_a)A_{Pass} \tag{20}$$
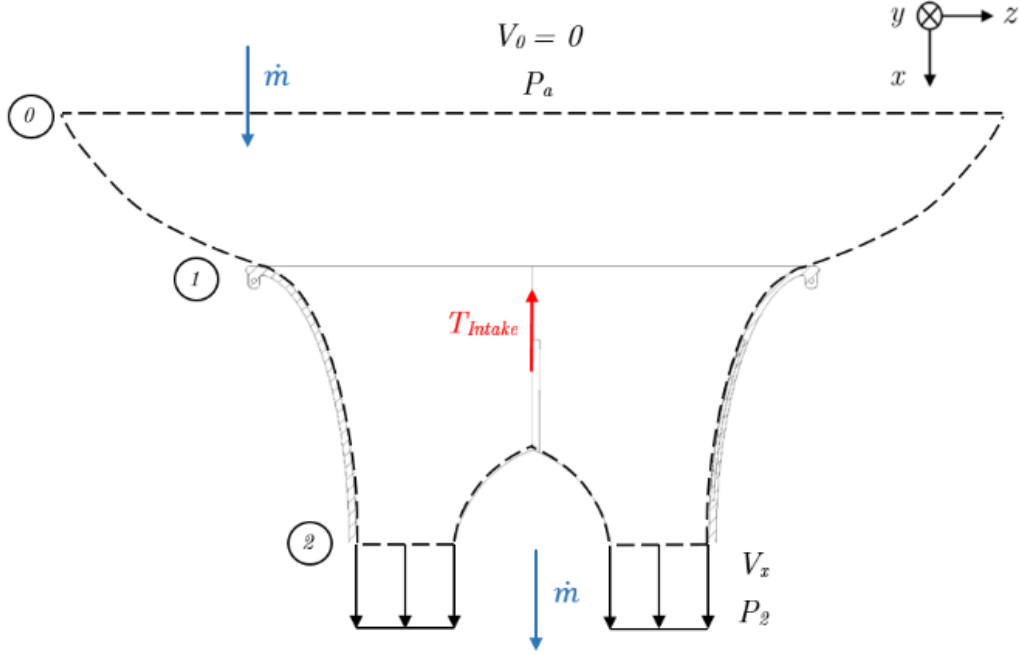

Figure 19: Control volume enclosing flow passing through the fan used to calculate intake thrust

The control volume enclosing the flow through the fan section of the ducted fan is shown in Figure 20. Application of the steady flow momentum equation gives Equation (21) for the fan thrust, T_{Fan}. The fan exit pressure, p_3 is calculated using the corrected pressure tapping measurement (Equation (14)).
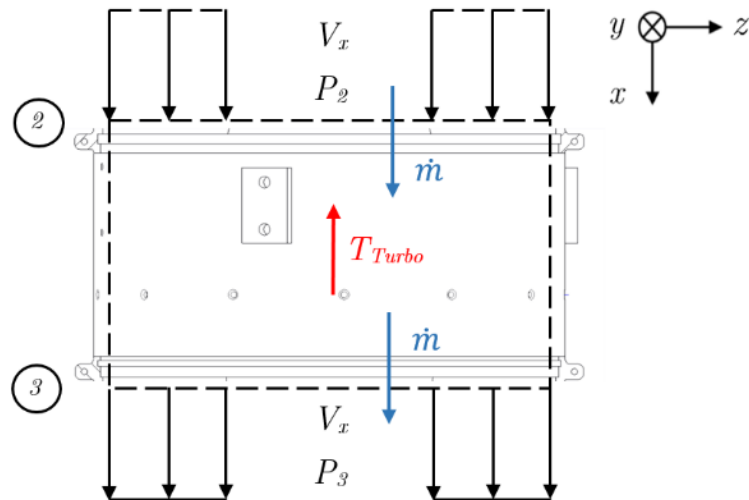

Figure 20: Control volume enclosing flow passing through the fan used to calculate fan thrust

$$T_{Fan} = \dot{m}V_x - \dot{m}V_x + (p_3 - p_2)A_{Pass} = (p_3 - p_2)A_{Pass} \tag{21}$$

The control volume enclosing the flow in the exit nozzle is shown in Figure 21 and the thrust contribution from the exit nozzle, T_{Exit} is then given by Equation (22). This expression is again found using the steady flow momentum equation, with the pressure forces calculated from numerical integration.

$$T_{Exit} = [pA]_{Exit,Nozzle} + [pA]_{Exit,Cone} + \dot{m}(V_x - V_j) + (p_3 - p_a)A_{Pass} \tag{22}$$
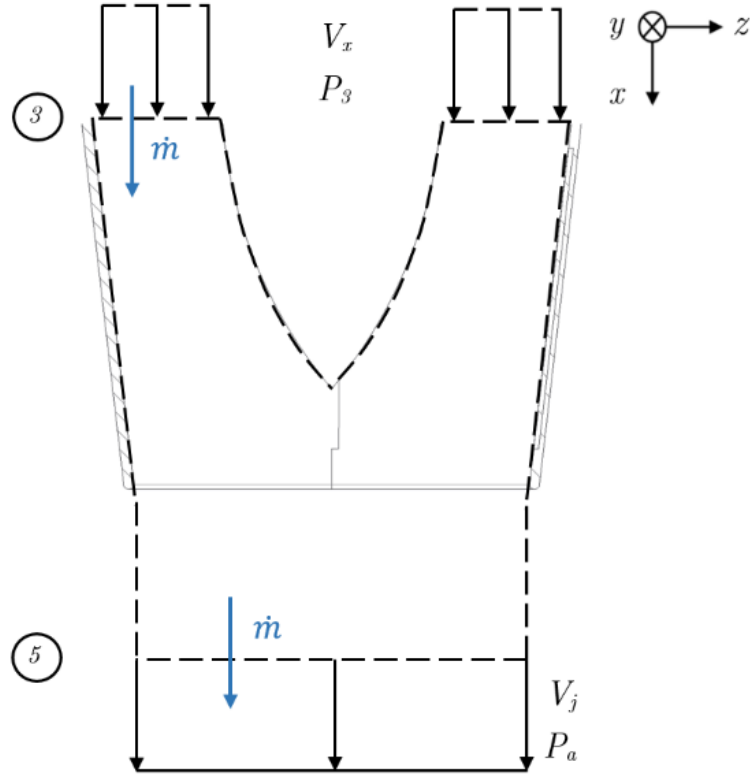

Figure 21: Control volume enclosing flow passing through the fan used to calculate exit nozzle thrust

The calculated thrust breakdown for the baseline intake and exit nozzle, including the total calculated thrust, $T_{T,Aero}$ and the value measured using the load cell is plotted in Figure 22. This shows that the calculated total thrust is 17.0% above the value measured from the load cell. It is hypothesised, that this is due to the control volume which encloses the captured stream-tube, assumes that this stream-tube does not have a stagnation point behind the lip of the intake. Another source of error is the pressure thrust acting on the intake cone, which was neglected.
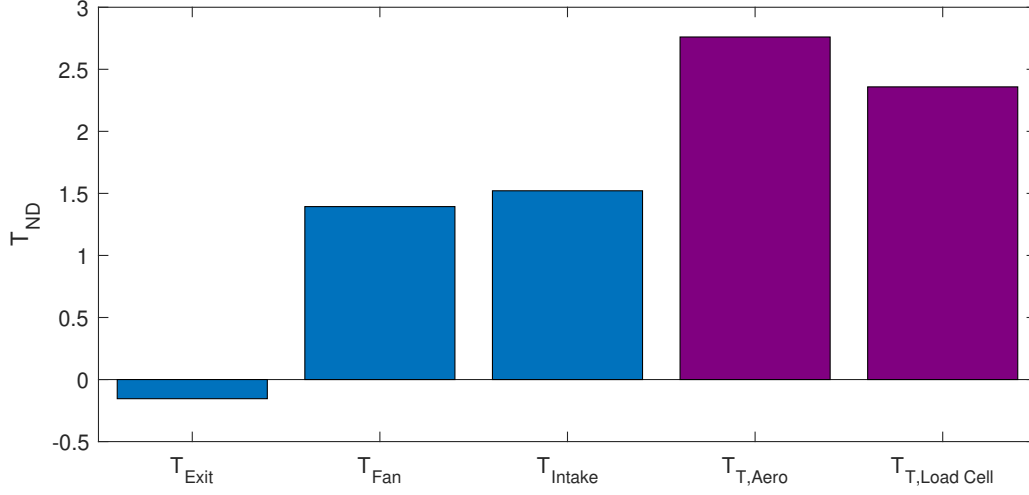
Figure 22: Measured non-dimensional thrust and the calculated contributions to the total non-dimensional thrust

The control volume method and momentum theory, which was used to calculate the theoretical non-dimensional figure of merit for an idealised ducted fan (Equation (5)), can also be used to calculate the breakdown of the total thrust [8]. It is therefore shown that proportion of the total thrust from the intake, fan and exit nozzle are given by Equations (23) to (25). These theoretical values, and those from the aerodynamic measurements, are summarised in Table 3. This shows that the proportions of the total thrust from the intake and the fan agree closely, and differ by less than 10%.

$$\frac{T_{Intake}}{T_T} = \frac{\sigma}{2} \tag{23}$$

$$\frac{T_{Fan}}{T_T} = \frac{1}{2\sigma} \tag{24}$$

$$\frac{T_{Exit}}{T_T} = \frac{-(\sigma - 1)^2}{2\sigma} \tag{25}$$

	Calculated	Theoretical
$\frac{T_{Intake}}{T_T}$	55.1%	42.7%
$\frac{T_{Fan}}{T_T}$	50.5%	58.6%
$\frac{T_{Exit}}{T_T}$	-5.62%	-1.3%

Table 3: Summary of the theoretical and calculated thrust breakdown

4 Modifications to the Exit Nozzle and Intake

Three exit nozzle designs were designed, all of which had a total length which was 19.4% of the baseline exit nozzle. This section details their design and measured performance.

4.1 Short Convergent Exit Nozzle

A short converging exit nozzle was tested with the geometry shown in Figure 8b, and was designed to have the same area ratio, σ as the baseline exit nozzle. However, the short exit nozzle was found to throttle the fan, reducing the flow coefficient to 0.48, which was hypothesised to be caused by constriction of the jet leaving the exit nozzle. Using the measured thrust, Equation (11) was used to calculate the area ratio of the exit jet to the annulus area. It is found that $\sigma = 0.71$, which is 17.3% below the design value, verifying this hypothesis.

4.2 Diffuser Design

To a design a diffusing exit nozzle, the ESDU design tables for annular diffusers are used [16]. For the sake of analysis, it is desired to have an exit nozzle design which has flow separation in the diffusing section, so that the effect of adding splitter vanes on the separation can be investigated. Therefore, the diffusing exit nozzle has an area ratio, $\sigma = 1.6$ as shown in Figure 8c, and is expected to have appreciable flow separation. A second design, which has an added splitter vane, is also shown in Figure 8d. This splitter is designed to separate the diffuser into two equal area annular diffusers. Whilst this split diffuser design is still expected to show flow separation, it is hypothesised that the splitter vane will reduce pressure loading on the outer wall of the exit nozzle, reducing the total drag from the exit nozzle.

When tested, the flow in both the diffusing exit nozzle and the split diffusing exit nozzle are found to separate between $\frac{x_{Exit}}{L_{Exit}} = 0$ and $\frac{x_{Exit}}{L_{Exit}} = 0.15$. This is clear from the flat regions the axial pressure profiles for the diffusing and split diffusing exit nozzles, which are shown in Figures 23 and 24 respectively.

For the split diffusing exit nozzle, the non-dimensional figure of merit is found to be 23.1% below that of the diffusing exit nozzle design. Therefore, this splitter design has not improved the performance and indicates that an optimised splitter design is required to delay flow separation and improve the performance.
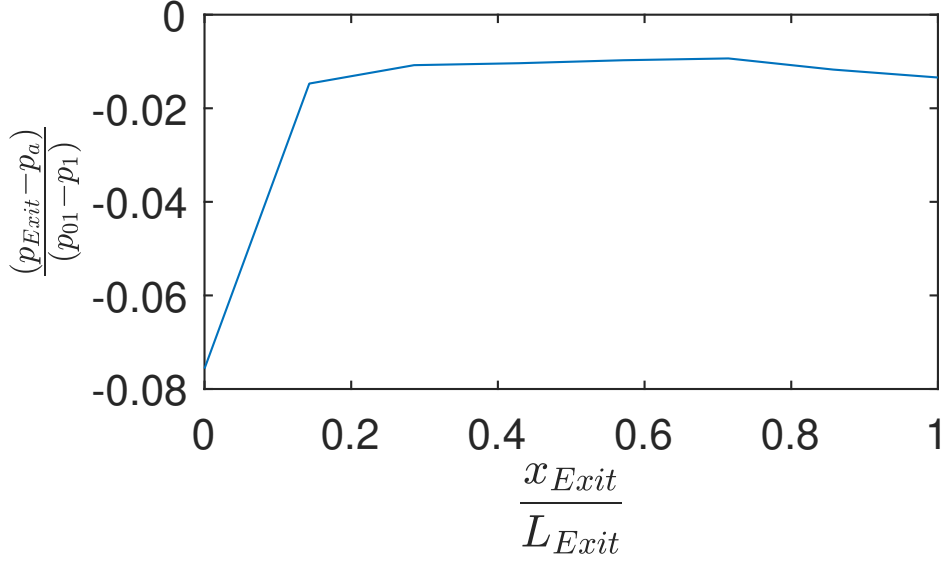
Figure 23: Axial static pressure profile measured on the diffusing exit nozzle

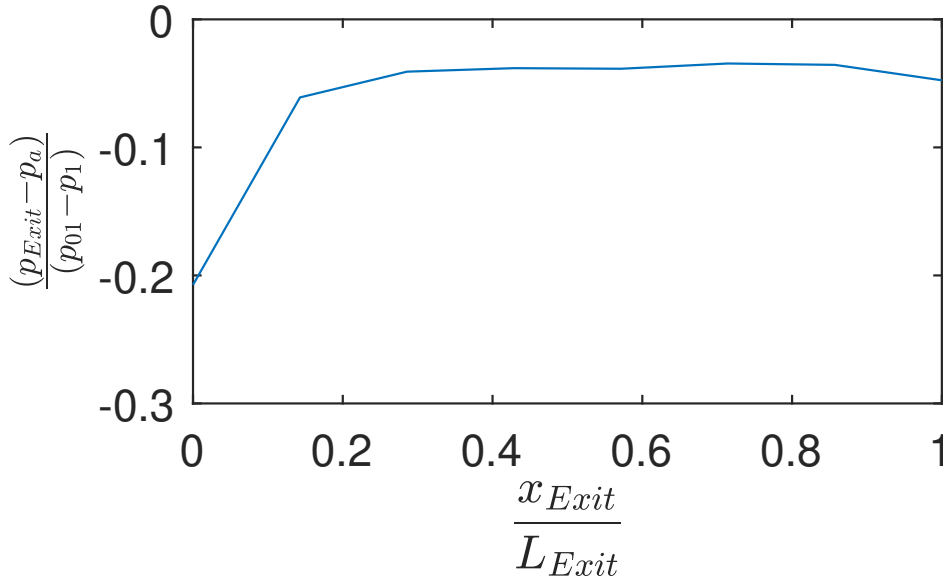Figure 24: Axial static pressure profile measured on the split diffusing exit nozzle

4.3   Modifications to the Intake

The reduced length intake design shown in Figure 7b, has a length which is 30% of the length of the baseline intake. The axial intake pressure profile for the short intake is shown in Figure 25, and the adverse pressure gradient for $\frac{x_{Intake}}{L_{Intake}} < 0.3$, indicates a large lip separation.
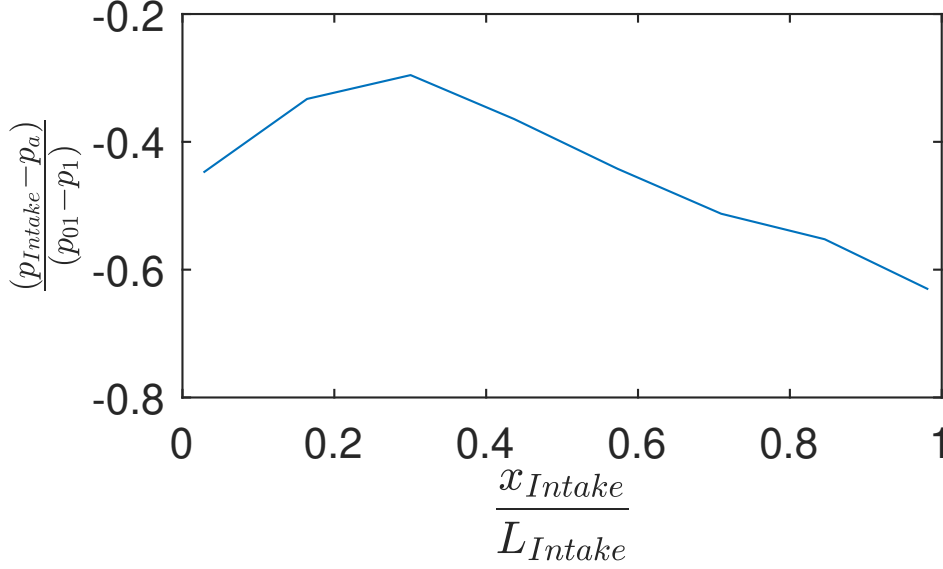
Figure 25: Axial static pressure profile measured on the short intake

When compared to the baseline intake, the intake thrust calculated from the measured pressure profile, T_{Intake} is found to decrease by 34.2%. The non-dimensional figure of merit $M_{f,Actual}$ is also found to decrease by 17.0%, and this is hypothesised to be due to the reduced intake thrust caused by the larger lip separation.

4.4 Combined Design Improvements

When testing the combined performance of the short intake and either of the diffusing exit nozzles, the flow coefficient can not be calculated using the current test rig. The high streamline curvature in the intake means that the flow coefficient cannot be calculated from the static pressure tapping at the fan inlet using Equation (9). Additionally, as the exit jet area is not known due to separation in the diffuser, the flow coefficient cannot be calculated using Equation (10). To correctly calculate the flow coefficient, the functionality of the rig can be extended to allow for additional measurements.

4.5 Rig Extensions

A calibrated multi-hole pressure probe, capable of moving in both the radial and circumferential directions, can be added to the entry and exit planes of the fan. This would allow the the flow coefficient to be calculated from the average measured axial velocity in these sections. Furthermore, the probes could also be used to calculate the static pressure rise across the fan allowing the isentropic efficiency to be calculated for all intake and exit nozzle designs.

As the speed frame on which the fan is mounted is reconfigurable, traverses could

be added with pressure probes both upstream of the intake and downstream of the exit nozzle. This would allow the jet velocity, V_j to be measured directly as well as the area of exit jet.

4.6   Comparison of Non-Dimensional Figure of Merit

To compare of the non-dimensional figure of merit when the operating point of the fan has changed, the isentropic efficiency of the fan for each test case is calculated. For all cases except the baseline intake and exit, the measured flow coefficient was used to calculate the isentropic efficiency by extrapolating the quadratic fit shown in Figure 18. This extrapolation was used because of the previously discussed issues in accurately calculating the stagnation pressure rise across the fan for these exit nozzle designs.

If the fan were redesigned so that the peak isentropic efficiency occurred at the new operating point, then the power to the fan would change to the adjusted value, P^* given by Equation (26). Furthermore, an adjusted non-dimensional figure of merit is then calculated with this adjusted power and is given by Equation (27). This method was applied to all other exit nozzle tests with the results summarised in Table 4.

$$P^* = P\left(\frac{\eta}{\eta^*}\right) \tag{26}$$

$$M_{f,Peak} = M_{f,Actual}\left(\frac{\eta^*}{\eta}\right) \tag{27}$$

Intake	Exit Nozzle	η	$M_{f,Actual}$	$M_{f,Peak}$	$M_{f,Theory}$
Baseline	Baseline	0.81	1.06	1.08	1.31
Baseline	Short	0.78	0.63	0.67	1.31
Baseline	Diffuser	0.71	0.93	1.08	1.79
Baseline	Split Diffuser	0.71	0.87	1.02	1.79
Short	Baseline	0.83	0.88	0.88	1.31
Short	Short	N/A	0.68	N/A	1.31
Short	Diffuser	N/A	0.91	N/A	1.79
Short	Split Diffuser	N/A	0.70	N/A	1.79

Table 4: Summary of the design combinations tested and the non-dimensional figures of merit

Comparing the adjusted non-dimensional figures of merit for each of the exit nozzle designs, the baseline exit nozzle and diffusing exit nozzle designs are found to have the highest VTOL efficiency, with $M_{f,Peak} = 1.08$. It is also seen that all of the adjusted non-dimensional figures of merit are below their theoretical values, with $M_{f,Peak}$ for the short converging exit nozzle calculated to be 48.9% below the theoretical value. This difference is hypothesised to be due to the real flow not being isentropic. In reality, there are losses caused by 3D edge separations, flows in the blade tip gaps and viscous effects.

The adjusted non-dimensional figure of merit for the baseline, diffusing and split diffusing exit nozzles are found to be greater than 1. These are therefore above the theoretical non-dimensional figure of merit for a propeller [8]. Another notable result is that the combined design of the short intake and the diffusing exit is found to have a figure of merit within 14.2% of that of the baseline case. Furthermore, this combination gives a reduction of 68.6% in the total duct weight, compared to the baseline intake and exit nozzle.

5 Conclusions

The following conclusions are made upon completion of this project:

1. The rig was successfully built, and with tests carried out at the design speed of 4000 RPM the baseline intake and exit nozzle case generates a total thrust of 26.4 N

2. The test rig can measure thrust, power, shaft speed and pressures across the whole casing, allowing the non-dimensional figure of merit, M_f to be calculated

3. Cases with converging nozzles, measured thrust from the load cell agrees within 20% of the value calculated from aerodynamic measurements

4. For the baseline case, the predicted breakdown of thrust shows $\approx 50\%$ of the measured thrust coming from each of the fan section and the intake, this matches the thrust decomposition predicted by a control volume analysis to within 10%

5. The combined design of short intake and diffusing exit is found to have a figure of merit within 14.2% of that of the baseline case, with a total reduction in weight of the intake and exit nozzle of 68.6%

6. To obtain the thrust decomposition for the design cases in which the pressure rise or the flow coefficient cannot be measured, a calibrated multi-hole probe traverse is needed at entrance and exit to the fan

6 Future Work

This section details the recommended future work to be undertaken using the test rig to improve the VTOL efficiency of the ducted fan designs.

6.1 CFD for Ducting Design

In order to design a diffusing exit nozzle with splitter vanes, it is recommended that CFD is used to analyse the diffuser flow. This would allow an optimised splitter design to be completed, which will ideally prevent separation in the exit nozzle. Similarly, CFD could be used to investigate the intake design of the intake to reduce or eliminate the thrust reductions caused by lip separation. With these combined improvements, a ducted fan design is expected to have a non-dimensional figure of merit which approaches the theoretical value.

6.2 Further Modifications

There are alternative methods to splitter vanes which could be used to delay flow separation in a diffusing exit nozzle which have not yet been tested, with one alternative being vortex generators.

6.2.1 Vortex Generators

Vortex generators are a simple yet highly effective form of boundary layer control used to delay or prevent separation [12], but they have minimal effect on the total pressure recovery of the intake. They generally take the form of small aerofoils fixed to the intake surface upstream of a separation region. The vortices have a centre of low pressure which is directed into to the target region to reduce the adverse pressure gradient, this in turn will delay or prevent flow separation.

This concept could be implemented in a ducted fan as illustrated in Figure 26, which shows how they may also be implemented to delay boundary layer separation in the exit nozzle. However, vortex generators are limited to wall angles $< 15°$ in their application to diffusers, and therefore for a fixed area ratio, σ the duct length can only be reduced to length which gives this diffuser profile angle.
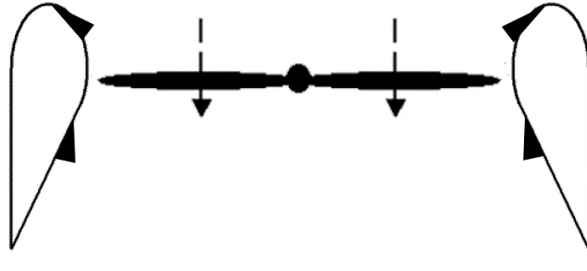
Figure 26: Example of a ducted fan implementing vortex generators

6.3 Cross-winds

It is found in the literature review that ducted fans are prone to separation at the intake, in the event of perturbations, such as a cross-wind. This separation causes a pitching moment due to ram drag [9], causing flight instability which is undesirable in a UAT.

By extending the rig to measure the load on all three of the load cells, once calibrated, they could be used to determine the magnitude and direction of the thrust vector. The rig could then be placed in a wind-tunnel, which could simulate the effect of a cross-wind on the ducted fan, and the comparative performance of different duct designs could be measured.

6.4 Noise

The noise of the propulsion is another important feature when selecting a propulsor for a UAT. This could be investigated for different duct designs by mounting a microphone on the test rig to measure the noise levels from different ducting designs for comparison.

A   Retrospective Evaluation of Risk Assessment

The risk assessment conducted at the beginning of the project led to the adoption safe practices and operating procedures. The primary risk is entrapment in the rotating components of the test rig, and this was greatly mitigated by their enclosure within the plastic casing of the working section. Furthermore, the operator sits away from the rig during operation with access to an emergency stop, further reducing risk of injury in the event of an unexpected failure.

B   Thrust Analysis

By assuming that the streamlines entering the control volume shown in Figure 13, the total momentum entering the control volume can be approxmiated using Equation (28).

$$\iint_{S_L} \rho(\underline{V_0} \cdot \mathbf{x})(\underline{V_0} \cdot \mathbf{z}) \, dS \approx V_0 \iint_{S_L} \rho(\underline{V_0} \cdot \mathbf{n}) \, dS = \dot{m}_L V_0 \tag{28}$$

Using this result, and applying the Steady flow momentum equation to the control volume in the axial direction, we obtain Equation (29) for the total thrust on the fan.

$$T_T = (p_a - p_a)A_5 + \dot{m}V_j + (\dot{m}_{Out,ext} + \dot{m}_L - \dot{m} + \dot{m}_{In,ext})V_0 \tag{29}$$

$$\Rightarrow T_T = \dot{m}(V_j - V_0) \tag{30}$$

C Numerical Integration of Pressure Forces

This section details the method of numerical integration used to calculate the axial force on a surface due to the static pressure acting normal to the surface. This was used to find the pressure force on the intake, exit nozzle and exit cone which are all cylindrically symmetric. The risk of blade failure was mitigated by an FEA analysis of the rotor blades during the previous summer research project, their enclosure in the casing, and careful clocking and balancing of the rotor. No blade rubbing was detected during testing.

For N pressure tappings distributed axially along a cylindrically symmetric, we can approximate the surface profile using M straight walled panels joining the locations of the tappings, where $M = N - 1$. Each of these n nodes has a known axial position, x_n and radial position, r_n as shown in Figure 27. This assumes that the surface is infinitesimally thin with the pressure difference acting across the surface at each of the N tappings, ΔP_n being known.
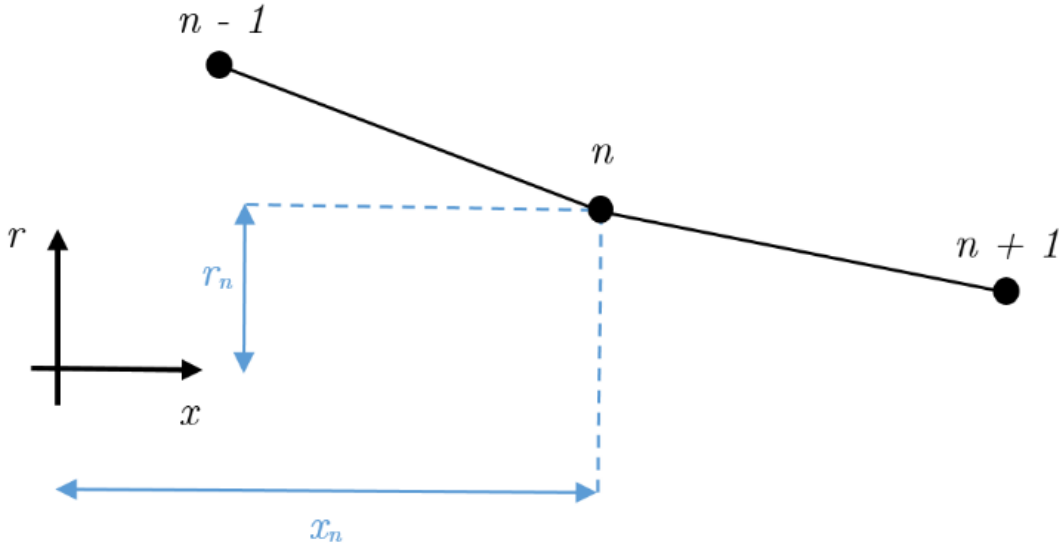

Figure 27: The approximate surface profile made from straight panels joining the static pressure tapping locations

We can then consider the profile of a single panel as shown in Figure 28, enclosed by two pressure tappings. The changes in axial position and radius across the panel, m are given by eqs. (31) and (32) respectively. The net of the area of the cylindrical panel is trapezoidal and can therefore be calculated using Equation (34). The pressure acting normal to the surface can be approximated by assuming it is the average pressure of the two pressure tappings enclosing it, as in Equation (35).

$$\Delta x_m = x_{m+1} - x_m \tag{31}$$

$$\Delta r_m = |r_m - r_{m+1}| \tag{32}$$

$$\theta_m = tan^{-1}\left(\frac{\Delta r_m}{\Delta x_m}\right) \tag{33}$$

$$A_m = 2\pi\left(\frac{r_m + r_{m+1}}{2}\right)(\Delta r_m^2 + \Delta x_m^2)^{0.5} \tag{34}$$

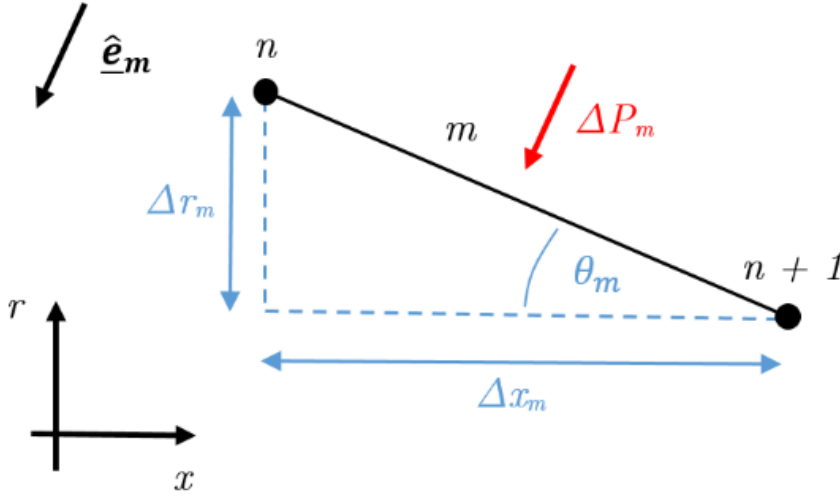$$\Delta P_m = \left(\frac{P_n + P_{n+1}}{2}\right) \tag{35}$$

Figure 28: The geometry of a panel section, m used in the numerical integration

The axial force contribution of each panel can be calculated by taking the dot product of the pressure force on the panel and the negative x direction (eq. (36)). Finally, the total axial pressure force on the surface, $T_{Pressure}$ is found by summing the contribution of each panel as in eq. (37).

$$T_m = (P_m A_m \hat{\underline{e}}_{\mathbf{m}}) \cdot (-\underline{\mathbf{i}}) = \Delta P_m A_m sin\theta_m \tag{36}$$

$$T_{Pressure} = \sum_{m=1}^{M} T_m \tag{37}$$

References

[1] Infrastructure and Projects Authority *National Infrastructure Delivery Plan 2016–2021*. URL https://assets.publishing.service.gov.uk, 2016.

[2] European Aviation Safety Agency (EASA) *EASA paves the way to enable safe air travel of urban air mobility and air taxi aircraft*. URL https://www.easa.europa.eu, 2018.

[3] Y. Ding, Z.P. Cano, A. Yu and J. Lu *Automotive Li-Ion Batteries: Current Status and Future Perspectives*. From the journal "Electrochemical Energy Reviews", 2019.

[4] BBC *Rolls-Royce develops propulsion system for flying taxi*. URL https://www.bbc.co.uk, 2018.

[5] B.W. McCormick, JR. *Aerodynamics of V/STOL Flight*. Academic Press, 1967.

[6] M.D. Patterson, J.M. Derlaga and N.K. Borer *High Lift Propeller System Configuration Selection for NASA's SCEPTOR Distributed Electric Propulsion Flight Demonstrator*. NASA, 2017.

[7] Advanced Research Division of Hiller Aircraft Corporation *Comparative Performance Charts for Ducted Propellers*. CUED, 2018.

[8] J.L. Pereira *Hover and Wind-tunnel Testing of Shrouded Rotors for Improved Micro Air Vehicle Design*. University of Maryland, 2008.

[9] H.W. Zhao *Development of a Dynamic Model of a Ducted Fan VTOL UAV*. RMIT University, 2009.

[10] C.J. Clark, G. Pullan, E. Curtis and F. Goenaga *Secondary Flow Control in Low Aspect Ratio Vanes Using Splitters*. URL http://turbomachinery.asmedigitalcollection.asme.org, 2017

[11] A. Dunlop *Super Aggressive S-Shaped Ducts for the SABRE Engine*. CUED, 2017.

[12] J. Seddon, E.L. Goldsmith *Intake Aerodynamics*. Blackwell Science Ltd., 1999.

[13] A. Maffiolo, C. Hall and S. Melvin *Aerodynamics of low reynolds number axial compressor sections*. 53rd AIAA Aersopace Sciences Meeting, 2015.

[14] I.C. Remfry et al. *Performance Improvements of Axial Diffusers for Incompressible Flow*. ESDU International, 1988.

[15] S.L. Dixon and C. Hall *Fluid Mechanics and Thermodynamics of Turbomachinery*. Elsevier, 2014.

[16] I.C. Remfry et al. *Performance of Circular Annular Diffusers Diffusers in Incompressible Flow.* ESDU International, 1988.

[17] N. Atkins *4A3: Turbomachinery I, Lecture Notes.* CUED, 2019.

[18] J. Barry *UROP: Compressor Stage for a Fan Test Rig* CUED, 2018.